Preference of Right-Handed Whistler Modes and Helicon Discharge Directionality due to Plasma Density Gradients

M. Granetzny,[1] O. Schmitz,[1] and M. Zepp[1]
University of Wisconsin - Madison, Department of Nuclear Engineering and Engineering Physics, WI, USA

(*Electronic mail: granetzny@wisc.edu)

(Dated: 19 August 2024)

Whistlers are magnetized plasma waves in planetary magnetospheres. Bounded whistlers, known as helicons, can create high-density laboratory plasmas. We demonstrate reversal of the plasma discharge direction by changing either antenna helicity or magnetic field direction. Simulations reproduce these findings only in the presence of a radial density gradient. Inclusion of such a gradient in the wave equation gives rise to azimuthal shear currents which for the first time consistently explains the preference of right- over left-handed whistlers and the discharge directionality in helicon plasmas.

Keywords: whistler, helicon, mode preference, handedness, density gradient, plasma waves, full wave simulation, LIF

Helicons[1,2] were discovered in the 1960s: first in solids[3,4], then plasmas[5–7], and identified as bounded whistler waves[8]. Whistlers are magnetized plasma waves and have been observed in the magnetospheres of Venus, Earth, Jupiter, Saturn, Uranus and Neptune[9,10]. How these waves can be used in terrestrial applications to generate and probe plasmas has been of general interest and subject to several decades of intensive research. Laboratory helicons are radio-frequency (RF) waves, typically at tens of MHz, and are well known for their ability to excite steady-state high density plasmas up into the 10^{20} m^{-3} range[11], directly from a cold gas. This capability can be highly beneficial to multiple fields of science and engineering including semiconductor-etching[12], advanced space propulsion[13], nuclear fusion materials testing[14,15] and plasma wakefield acceleration[11,16]. Their widespread occurrence in nature and the large range of applications makes understanding the confinement and directionality of these waves a high priority. Helicons are therefore of major interest inside the broader field of low-temperature plasma physics[17,18].

Whistler waves propagating along a magnetic field in an unbounded homogeneous plasma are R-waves[19] and as such right-hand polarized. However, whistler modes in bounded plasmas, such as laboratory helicons or ducted magnetospheric whistlers[20,21], form mode patterns that can rotate in a left-handed or right-handed sense around the guiding magnetic field[22]. Experiments have shown a predominance of right- over left-handed whistler modes[23]. Moreover, experiments using half-helical antennas[24], which are known to produce the highest plasma density, have shown a strong directionality of the plasma discharge[25]. However, neither observation could ever be explained satisfactorily. We present here for the first time the reason for both effects and how they relate to each other. In Fig. 1, the plasma directionality is demonstrated at the MAP experiment, shown later in Fig. 2. Density profiles and optical emission show that a right-helical antenna - a half-helical antenna with right-handed helicity - in a rightward magnetic field generates a leftward discharge (blue case). In a leftward field the discharge is rightward (green). For a left-helical antenna the discharge is to the right for a rightward field (orange) but to the left for a leftward field

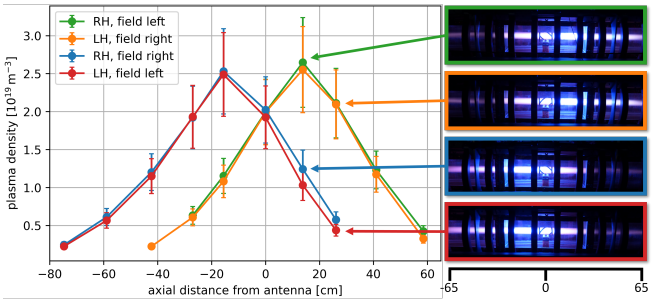

FIG. 1. Dependence of the helicon plasma density and light emission on the antenna helicity - left-helical (LH) or right-helical (RH) - and background magnetic field direction - leftward or rightward in this figure.

(red). These measurements reveal that the discharge can be directed by changing the magnetic field direction or antenna helicity, resulting in identical but axially mirrored profiles. Starting from this observation, we demonstrate in this paper for the first time that radial density gradients enhance or attenuate whistler modes based on their handedness. For radially peaked density profiles this results in the preference of right-handed modes which in turn leads to the observed discharge directionality. This mechanism is fundamental to the coupling of whistler modes to magnetized plasmas with radial density gradients in solid-state, gaseous laboratory, and magnetospheric plasmas.

Over the years numerous groups have studied half-helical antennas with right- and left-handed helicity and found that the former produce higher plasma densities than the latter[22,25]. However, all those studies were performed in experiments with complicating effects due to the vacuum vessel or magnetic field geometry. The most common case is the excitation of helicon waves close to the axial boundary of the vacuum vessel[5,24–30], which introduces axially asymmetric boundary conditions around the antenna and can lead to discharges being launched directly into a nearby vacuum wall. In addition many experiments employ expansion chambers downstream of the helicon excitation region[31–35], resulting in strong axial

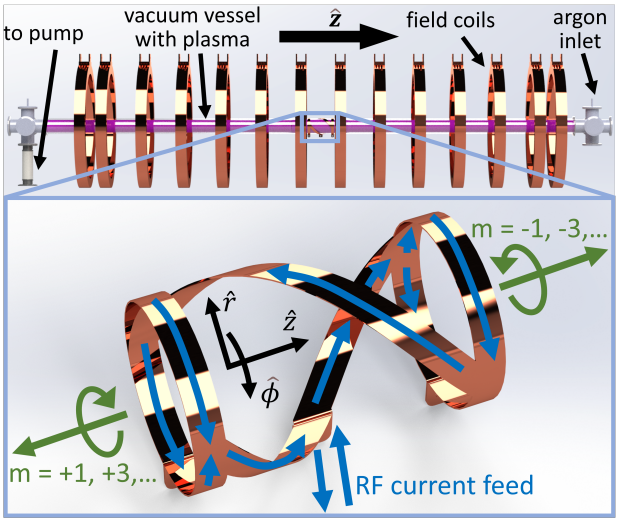

FIG. 2. Top: CAD model of the core components of the MAP experiment. Bottom: Right-half-helical antenna with currents during one half of the RF cycle in blue and axial launch and azimuthal rotation directions for the different modes in green.

density gradients. Another common setup features strong gradients in the axial magnetic field[32,35–38]. Inferring the reasons for the discharge directionality and preference of right-handed modes is difficult in these setups because the helicon dispersion relation depends strongly on the magnetic field strength and plasma density. To our knowledge no experimental investigation of the discharge directionality has been conducted in a setup without these complicating effect, thus the effect of field direction and antenna helicity on the discharge direction in Fig. 1 has not been demonstrated before. For the experiments presented here we generated the helicon discharge from the center of a long vacuum vessel, with significant distance to both axial boundaries, and inside a highly homogeneous field.

The experiments were performed at the Madison AWAKE Prototype (MAP), shown in Fig. 2. MAP consists of a 2 m long borosilicate glass tube with an ID of 52 mm and an OD of 56 mm. 14 coils produce a very homogeneous magnetic field of 49 mT in the central 1.6 m of the device, reaching 55 mT at the ends. A 10 cm long antenna with 1 cm wide straps, shown in the lower panel of Fig. 2, is wound in either a right- or left-helical sense and used to excite the helicon plasma. The right-half-helical antenna shown launches both right- and left-handed azimuthal modes, with mode numbers m, in the indicated directions[37]. Notably, a whistler mode's handedness can be uniquely defined relative to the background magnetic field. In a field pointing along $\hat{z}$ in Fig. 2 positive m modes are right-handed and negative m modes are left-handed. Importantly, a left-helical antenna reverses the axial launch directions, making negative m modes right-handed and positive m modes left-handed.

All experiments were performed at an argon fill pressure of 10^{-2} mbar with RF input power set to 1.3 kW at 13.56 MHz. An impedance matching network was used to reduce reflected power to negligible levels of less than 10 W. Plasma breakdown was readily achieved at $\omega_{RF}/\omega_{ce} = 9.89 \cdot 10^{-3}$ and $B/n_n = 1.98 \cdot 10^5$ Hx[39], where ω_{ce} and n_n are the electron-cyclotron frequency and initial neutral gas density, respectively. The plasma density was measured by means of laser-induced fluorescence (LIF) on singly ionized argon. The LIF diagnostic is nearly identical to the LIF system used to study helicons in the MARIA device[27,40]. The diagnostic is designed around a 40 mW tunable diode laser, amplified to a maximum of 500 mW. The laser excites the argon ion transition at 668.614 nm from the $3d^4F_{7/2}$ state to the $4p^4D_{5/2}$ state, which then decays with an emission at 442.6 nm to the $4s^4P_{3/2}$ state within nanoseconds. The laser is linearly polarized and injected radially into MAP. Movable collection optics with a radial line of sight at a 90° angle to the injected beam collect the fluorescent light and deliver it to a photo-multiplier tube. Subsequently the fluorescence signal is extracted with a lock-in amplifier. In addition, photographs of the discharges were taken.

The results were shown previously in Fig. 1. They show that reversal of either the antenna helicity or background field direction reverses the discharge direction and reversal of both restores the original discharge direction. The matching network settings used were identical for all four cases and resulted in less than 10 W reflected power for each of them. This observation indicates identical plasma impedance across all four discharges. These results were obtained with very good magnetic field homogeneity and proper distance to axial vacuum boundaries. They therefore remove ambiguities in the interpretation of measurements by other groups due to their experimental setups, such as placement of the antenna close to an axial boundary or near regions with plasma density or field strength outside the values allowed by the dispersion relation[41].

Helicon discharges in MAP were modelled using a quasi-3D finite element model developed in COMSOL using the cold plasma wave description. In a high density helicon plasma a significant part of the power is deposited by the Trivelpiece-Gould mode[42] which has very short radial wavelength on the sub-mm scale. This necessitates use of very fine mesh elements of 500 μm axially and 30 μm radially. The model assumes that wavefields have an $e^{im\phi}$ dependence in the azimuthal direction. Due to strong damping of higher order modes, a full 3D solution can be calculated from the six leading order azimuthal modes, namely $m = \{\pm 1, \pm 3, \pm 5\}$. Power deposition is calculated strictly ohmically through electron-ion and electron-neutral collisions since Landau damping is negligible[43]. The model was verified by comparing results in a homogeneous plasma against the analytical helicon dispersion relation[41].

Plasma temperature and neutral pressure were set to be uniform at 3 eV and 10^{-3} mbar, respectively, the latter assuming a 90% neutral depletion. Density profiles used in the simulation were interpolated from 86 local LIF measurements in a plasma generated by a right-helical antenna in a leftward field (green case in Fig. 1). The results of this simulation are shown in Fig. 3. The upper panel shows the magnitude of the total wave magnetic field, with plasma density indicated by white contour lines. The helicon wave propagates radially in-

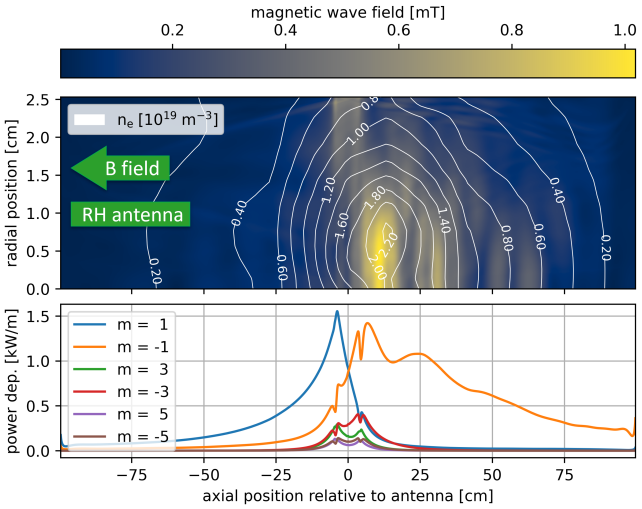

FIG. 3. Simulation results for an RH antenna with magnetic field in the negative $\hat{z}$ direction, representing the green case in Fig. 1. Top: Measured plasma density and simulated wave magnetic field strength. Bottom: Axial power deposition by azimuthal modes.

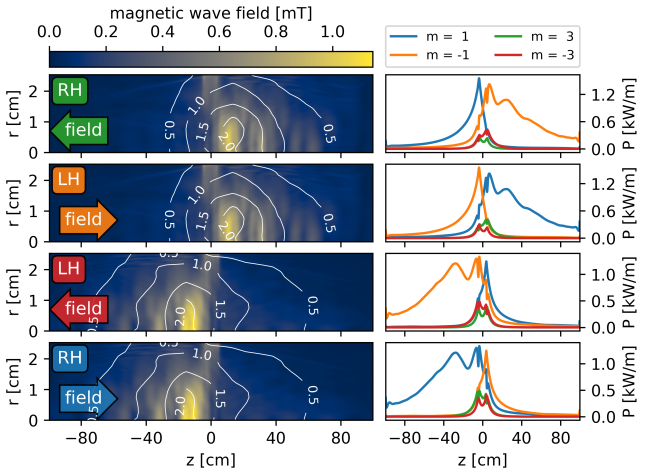

FIG. 4. Comparison of simulation results for the four combinations of antenna helicity and magnetic background field direction, representing the green, orange, red and blue cases in Fig. 1. White contour lines show plasma density in units of 10^{19} m^{-3}.

wards and axially rightward from the antenna location. The lower panel shows the radially integrated power deposition contributions from the different azimuthal modes. Azimuthal modes with negative mode numbers (-1, -3, ...) deposit power predominantly to the right, while positive modes (1, 3, ...) deposit power mostly to the left. This is in agreement with the azimuthal mode launch directions for these modes as indicated in Fig. 2. In this setup the dominant right-handed mode, $m = -1$, deposits 58.7% of the total power, mostly to the right, while the leading left-handed mode, $m = +1$, deposits 29.5% of the total power, mostly to the left. The remaining 11.8% are accounted for by higher order modes. Overall the power deposition is dominated by the leading right-handed mode and shows the same directionality observed optically and by LIF in Fig. 1 (green case).

A comparison of simulation results for all four combinations of antenna helicity and background field direction is shown in Fig. 4. The density profiles shown were measured for a right-handed antenna with both leftward and rightward pointing background fields. Due to the symmetry shown experimentally in Fig. 1, these density profiles were used for simulating the wave propagation from left-handed antennas as well. As expected from our experiments these simulations show a reversal of the wavefield propagation direction and power deposition patterns if either the background field or antenna helicity is reversed. The power deposition is dominated by either the $m = 1$ or $m = -1$ azimuthal modes, depending on which is the right-handed mode with respect to the background field direction. As mentioned earlier reversal of the antenna helicity reverses the launch directions for these azimuthal modes.

To shed light on the reason for the directional power deposition we performed simulations with axially uniform plasma density profiles. The radial plasma density profiles were either modelled as a flat top of the form[44]

$$n_e = \left(n_e^{peak} - n_e^{edge}\right)\left[1 - \left(\frac{r}{r_w}\right)^5\right]^5 + n_e^{edge}, \qquad (1)$$

with $n_e^{peak} = 2.5 \cdot 10^{19}$ m^{-3}, $n_e^{edge} = 5.0 \cdot 10^{18}$ m^{-3} and vacuum wall location $r_w = 26$ mm or with a constant density of $n_e = 2.5 \cdot 10^{19}$ m^{-3} throughout.

Results for the four combinations of antenna helicity and field direction for both profiles are shown in Fig. 5. For a radial density gradient and a rightward field with an right-helical antenna, or a leftward field with an left-helical antenna, the power deposition is predominantly to the left. For the other two combinations, the power deposition is predominantly to the right. The left-right power imbalance is 36.5% to 63.5%. For the radially homogeneous plasma no significant preferential power deposition exists, with the left-right imbalance being only 48.1% to 51.9%.

Measurements and simulations show qualitatively the same effect of antenna helicity and magnetic field direction on the discharge direction. We have shown computationally that, even in an axially homogeneous plasma, a radial density gradient leads to a preferential direction for axial power deposition. However, the power deposition becomes symmetric when no radial density gradient is present. An understanding of this phenomenon can be gained by deriving the helicon wave equation for a plasma with a purely radial density gradient. We follow Chen's approach[41] who derives the wave equation for a completely homogeneous plasma. Wave fields are assumed to be sinusoidal in the azimuthal and axial directions, i.e. they are of the form $e^{i(m\phi + kz - \omega t)}$, where k is the axial wavenumber and ω the wave frequency. In helicon plasmas the electron currents are far stronger than the displacement currents and the ions are immobile, hence the relevant

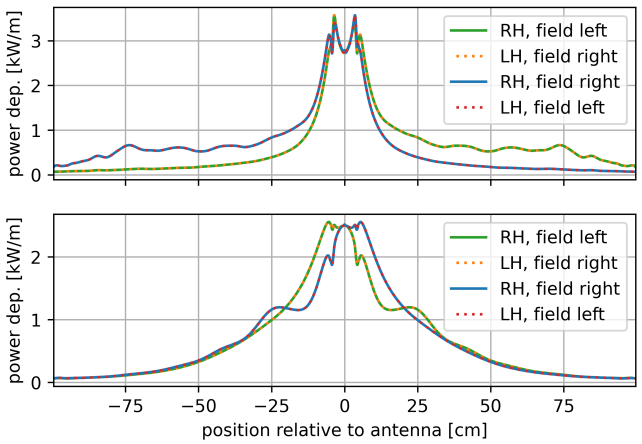

FIG. 5. Simulated power deposition profiles for helicon discharges with different field directions and antenna helicities in plasmas with radial density gradient (top) and uniform density (bottom). Green and orange as well as blue and red curves are overlapping, respectively.

Maxwell equations in the frequency domain become

$$\nabla \times \boldsymbol{E} = i\omega \boldsymbol{B} \tag{2}$$
$$\nabla \times \boldsymbol{B} \approx \mu_0 \boldsymbol{j} \approx -\mu_0 e n \boldsymbol{v}, \tag{3}$$

where the incompressible electron fluid has density n and velocity $\boldsymbol{v}$. The electrons are subject to electric, magnetic, friction and pressure gradient forces such that their momentum equation becomes

$$-i\omega m_e \boldsymbol{v} = -e(\boldsymbol{E} + \boldsymbol{v} \times \boldsymbol{B_0}) - m_e \nu \boldsymbol{v} - \frac{k_b T_e}{n} \nabla n, \tag{4}$$

where $\boldsymbol{B_0}$ is the background magnetic field, T_e is the electron temperature and ν is an effective combined electron-ion and electron-neutral collision frequency.

As shown in the appendix, we can use this set of equations to eliminate $\boldsymbol{E}$, $\boldsymbol{j}$ and $\boldsymbol{v}$ and arrive for purely radial density gradients at

$$\begin{aligned} &\delta \nabla \times \nabla \times \boldsymbol{B} \mp k \nabla \times \boldsymbol{B} + k_w^2 \boldsymbol{B} \\ &= \delta \frac{\nabla n}{n} \times (\nabla \times \boldsymbol{B}) \mp i \left[\frac{\nabla n}{n} \cdot (\nabla \times \boldsymbol{B}) \right] \hat{\boldsymbol{z}}, \end{aligned} \tag{5}$$

where we have used the definitions

$$\delta = \frac{(\omega + i\nu) m_e}{e B_0} \quad \text{and} \quad k_w^2 = \frac{\mu_0 e n \omega}{B_0}. \tag{6}$$

In Eq. 5 the $\mp$ sign accounts for pointing of the background magnetic field either along or against $\hat{\boldsymbol{z}}$. The left-hand side of Eq. 5 is the helicon wave equation in a homogeneous plasma[41]. The terms on the right-hand side exist only in the presence of a density gradient; we will hereafter refer to them as the modulating magnetic field as explained below. Since δ is the ratio of the RF frequency to the electron cyclotron frequency, the first term on the right-hand side of Eq. 5 is negligible and the modulating magnetic field becomes

$$\mp i \left[\frac{\nabla n}{n} \cdot (\nabla \times \boldsymbol{B}) \right] \hat{\boldsymbol{z}} \approx \pm \frac{m B_z}{n r} \frac{\partial n}{\partial r} \hat{\boldsymbol{z}}, \tag{7}$$

where the right-hand side exploits that r becomes small towards the plasma core where the density is highest such that the B_z term of $\nabla \times \boldsymbol{B}$ dominates.

This form shows very clearly a dependence on the magnetic field direction, density gradient and azimuthal mode number. For a background field along $\hat{\boldsymbol{z}}$ and a radially inward density gradient, the additional modulating magnetic field enhances positive but attenuates negative m modes, which explains the preference of right-handed over left-handed modes. Moreover, since helical antennas of opposite helicity send those modes in opposite directions this explains the directionality of helicon discharges and why helicity or field reversal flip the discharge direction. This mechanism also explains the remaining power imbalance in the homogeneous plasma case in Fig. 5. In our model the antenna launches waves at the outside of the vacuum vessel which has a wall thickness of 2 mm. This represents an effective very steep radial plasma density gradient from the launch region into the plasma edge. The result is a very strong attenuation of left-handed modes in this transition region which leads to a high power deposition close to the antenna. As the waves propagate radially further inward and axially away from the launch region the power deposition becomes symmetric again as the radial plasma density gradient is zero in the homogeneous plasma case.

The significance of the modulating magnetic field relative to the wave dynamics in a uniform plasma becomes clear by comparing the $k\nabla \times \boldsymbol{B}$ term in Eq. 5 to the dominant source term $\frac{\nabla n}{n} \cdot (\nabla \times \boldsymbol{B})$. Their ratio, i.e. $\frac{\nabla n}{n}/k \approx (rk)^{-1}$, is 63%, where we have used the vessel radius $r = 26$ mm and an axial wavenumber $k = 2\pi/(10\,\text{cm})$ defined by the antenna length. The density gradient thus results in a significant change in the wave dynamics. Importantly the derivation of the wave equation makes no assumption on the strength of the background magnetic field apart from that it should result in the whistler wave frequency being much smaller than the electron-cyclotron frequency such that we have $\delta \ll 1$. For example at our RF frequency of 13.56 MHz this assumption would still be valid down to a field of just 5 mT resulting in a ratio of 0.1.

The physical mechanism behind modulating magnetic field can be understood by using Eq. 3 to bring the wave equation into the form

$$\delta \nabla \times \nabla \times \boldsymbol{B} \mp k \nabla \times \boldsymbol{B} + k_w^2 \boldsymbol{B} = \mp \frac{i\mu_0}{n} \frac{\partial n}{\partial r} j_r \hat{\boldsymbol{z}}, \tag{8}$$

which shows that radial wave currents (j_r) in conjunction with the field direction and density gradient are responsible for the additional modulating magnetic field which has a $\mp 90°$ phase shift relative to j_r.

A physical explanation of the modulating field is given in Fig. 6. In a background field along $\hat{\boldsymbol{z}}$ an electron fluid element carrying a radial current j_r is subject to a Lorentz force

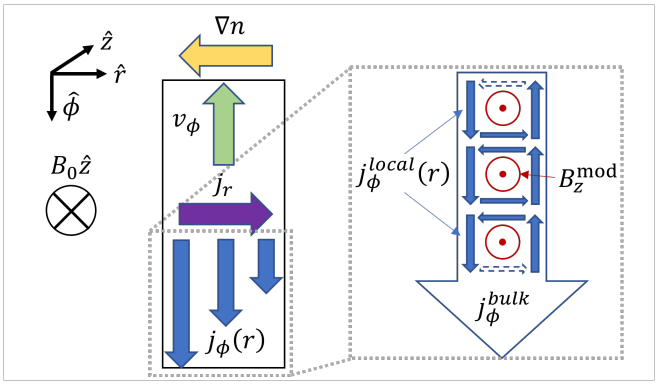

FIG. 6. Mechanism behind the modulating magnetic field in the presence of a radial density gradient.

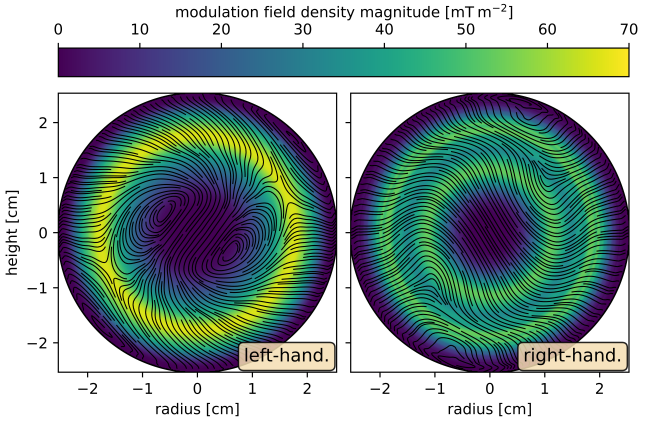

FIG. 7. Magnitude of the modulating magnetic field and wave magnetic field lines for the leading left-handed and right-handed modes.

that induces a fluid flow (v_ϕ) which in turn represents an azimuthal current j_ϕ. This current experiences a Lorentz force as well, resulting in a current in the negative radial direction. This is the mechanism by which helicon waves exchange energy between radial and azimuthal currents in a homogeneous plasma. However, in the presence of an electron density gradient (∇n) neighboring fluid elements will carry azimuthal currents with magnitudes proportional to the electron density, leading to an azimuthal shear current. These currents can be described by a bulk current plus local currents for the different radial positions. The local parts represent dipole currents which create a magnetic field in the $\pm\hat{z}$ direction which we have expressed mathematically by the modulating magnetic field in Eq. 8. For a right-handed helicon mode in a homogeneous plasma the j_r currents lead j_ϕ by 90°. In the case of a radially inward density gradient, the modulating field then points along the mode's regular B_z field and leads to an enhancement of the wavefields. In contrast a left-handed mode has j_r lagging j_ϕ by 90° such that the additional modulating field results in B_z wavefields in the wrong direction, thereby attenuating j_r, j_ϕ and the wave overall. In a hollow plasma channel, such as density troughs guiding magnetospheric whistler waves[8], the same mechanism would lead to an enhancement of left- over right-handed modes.

The modulating magnetic field results in a distortion of the left- and right-handed mode patterns compared to those in a homogeneous helicon plasma. This is demonstrated in Fig. 7 which shows cross sections of the leading left- and right-handed mode magnetic wave fields superimposed on the magnitude of the modulating field. The enhancement of the right-handed mode is visible by a lack of vortices that are normally present in such modes[45] in addition to a general dragging of the field lines in the direction of rotation for this mode, i.e. in this view counterclockwise. For the left-handed mode the strength of vortices is increased and we find regions of field reversal at the radial locations with strong modulation fields. Field lines are dragged counterclockwise as well which is against the direction of rotation for this mode.

We have shown experimentally, computationally and analytically that radially inward density gradients enhance right- but attenuate left-handed whistler modes. This mechanism explains long standing observations of preferential excitation of right-handed whistler modes and consequently the directionality of helicon plasmas generated by helical antennas. The discharge direction is defined by the combination of antenna helicity and magnetic background field direction. Measurements show that all four combinations of helicity and field direction produce identical discharges with the only difference being an axial mirroring around the antenna location. We have demonstrated that radial density gradients induce azimuthal shear currents which in turn generate a modulating magnetic field that interferes with the axial component of the whistler wave fields. The opposite phasing of currents in right- and left-handed whistler modes results in the modulating field amplifying the former but attenuating the latter. Since helical antennas of opposite helicity send right- and left-handed modes in opposite directions, changing the helicity changes the discharge direction. Moreover, since right- or left-handedness of a mode with a given spatial rotation direction depends on the direction of the background field, the discharge is reversed when the field direction is reversed. In a broader context, the discovered mechanism predicts preference of left-handed modes in hollow plasma channels and is fundamental to the wave-plasma coupling of whistler modes in general, for example in solids and planetary magnetospheres.

We would like to express our gratitude to Barret Elward for his outstanding work during the construction of the MAP experiment. We would also like to thank Dieter Boeyaert, Kelly Garcia, Madelynn Knilans, Carl Sovinec and Danah Velez for their feedback on the manuscript. The research presented here was funded by the National Science Foundation under grant PHY-1903316 and NSF-CAREER award PHY-1455210 as well as the College of Engineering at UW-Madison.

AUTHOR DECLARATIONS

Conflict of Interest

The authors have no conflicts to disclose.

Author Contributions

Marcel Granetzny: Conceptualization (lead); Data curation (lead); Formal analysis (lead); Investigation (lead); Methodology (lead); Project administration (equal); Software (lead); Validation (equal); Visualization (lead); Writing - original draft (lead); Writing - review & editing (lead). **Oliver Schmitz:** Conceptualization (equal); Funding acquisition (lead); Project administration (equal); Resources (lead); Supervision (lead); Writing - original draft (supporting); Writing - review & editing (supporting). **Michael Zepp:** Data curation (equal); Formal analysis (equal); Investigation (equal); Methodology (equal); Software (equal); Validation (equal); Writing - review & editing (supporting).

DATA AVAILABILITY

The data that support the findings of this study are available from the corresponding author upon reasonable request.

Appendix A: Derivation of the Wave Equation in a Plasma with Radial Density Gradient

The plasma is assumed to be inhomogeneous only in the $\hat{\boldsymbol{r}}$ direction such that any wavefields $\boldsymbol{W}$ are of the form

$$\boldsymbol{W} = \boldsymbol{W_0}(r) e^{i(m\phi + kz - \omega t)}. \tag{A1}$$

Azimuthal and axial derivatives then simplify to

$$\frac{\partial \boldsymbol{W}}{\partial \phi} = im\boldsymbol{W}, \tag{A2}$$

and,

$$\frac{\partial \boldsymbol{W}}{\partial z} = ik\boldsymbol{W}. \tag{A3}$$

We will express the axial background magnetic field as

$$\boldsymbol{B_0} = sB_0\hat{\boldsymbol{z}} \quad \text{with} \quad B_0 = |\boldsymbol{B_0}|, \tag{A4}$$

where $s = \pm$ indicates alignment along or against $\hat{\boldsymbol{z}}$, respectively.

Using this expression in the electron momentum equation (Eq. 4) we get after some rearranging

$$\boldsymbol{E} = B_0 \left[s\hat{\boldsymbol{z}} \times \boldsymbol{v} + i\frac{(\omega + i\nu) m_e}{eB_0} \boldsymbol{v} \right] - \frac{k_b T_e}{en} \boldsymbol{\nabla} n. \tag{A5}$$

We can now substitute $\boldsymbol{E}$ into Faraday's law (Eq. 2) and define $\delta = (\omega + i\nu) m_e / (eB_0)$ to arrive at

$$i\omega \boldsymbol{B} = B_0 \boldsymbol{\nabla} \times (s\hat{\boldsymbol{z}} \times \boldsymbol{v} + i\delta \boldsymbol{v}) - \frac{k_b T_e}{e} \boldsymbol{\nabla} \times \frac{\boldsymbol{\nabla} n}{n}. \tag{A6}$$

By the chain rule we have

$$\boldsymbol{\nabla} \left(\frac{1}{n} \right) = -\frac{1}{n^2} \boldsymbol{\nabla} n, \tag{A7}$$

and the last term in Eq. A6 vanishes since

$$\boldsymbol{\nabla} \times \frac{\boldsymbol{\nabla} n}{n} = \frac{\boldsymbol{\nabla} \times \boldsymbol{\nabla} n}{n} - \frac{\boldsymbol{\nabla} n \times \boldsymbol{\nabla} n}{n^2} = 0. \tag{A8}$$

Further, by expressing $\boldsymbol{v}$ through $\boldsymbol{B}$ using Eq. 3, we can transform Eq. A6 into

$$i\omega \boldsymbol{B} = -\frac{B_0}{\mu_0 e} \boldsymbol{\nabla} \times \left\{ \frac{1}{n} \left[s\hat{\boldsymbol{z}} \times (\boldsymbol{\nabla} \times \boldsymbol{B}) + i\delta \boldsymbol{\nabla} \times \boldsymbol{B} \right] \right\}. \tag{A9}$$

After applying the chain rule and Eq. A7, Eq. A9 becomes

$$\begin{aligned} \frac{i\mu_0 en\omega}{B_0} \boldsymbol{B} = \quad & -s\boldsymbol{\nabla} \times [\hat{\boldsymbol{z}} \times (\boldsymbol{\nabla} \times \boldsymbol{B})] \\ & -i\delta \boldsymbol{\nabla} \times (\boldsymbol{\nabla} \times \boldsymbol{B}) \\ & + \frac{s}{n} \boldsymbol{\nabla} n \times [\hat{\boldsymbol{z}} \times (\boldsymbol{\nabla} \times \boldsymbol{B})] \\ & + \frac{i\delta}{n} \boldsymbol{\nabla} n \times (\boldsymbol{\nabla} \times \boldsymbol{B}). \end{aligned} \tag{A10}$$

By using the vector identity for the curl of a cross product, we can expand the first term in Eq. A10 into four parts, namely

$$\begin{aligned} \boldsymbol{\nabla} \times [\hat{\boldsymbol{z}} \times (\boldsymbol{\nabla} \times \boldsymbol{B})] = \quad & \hat{\boldsymbol{z}} [\boldsymbol{\nabla} \cdot (\boldsymbol{\nabla} \times \boldsymbol{B})] \\ & - (\boldsymbol{\nabla} \times \boldsymbol{B}) (\boldsymbol{\nabla} \cdot \hat{\boldsymbol{z}}) \\ & + [(\boldsymbol{\nabla} \times \boldsymbol{B}) \cdot \boldsymbol{\nabla}] \hat{\boldsymbol{z}} \\ & - (\hat{\boldsymbol{z}} \cdot \boldsymbol{\nabla}) (\boldsymbol{\nabla} \times \boldsymbol{B}). \end{aligned} \tag{A11}$$

Since the divergence of a curl is zero and $\hat{\boldsymbol{z}}$ is constant, the first three terms in Eq. A11 vanish. The last term can be calculated as

$$\begin{aligned} -(\hat{\boldsymbol{z}} \cdot \boldsymbol{\nabla}) (\boldsymbol{\nabla} \times \boldsymbol{B}) = \quad & -\mu_0 \left(\hat{\boldsymbol{r}} \frac{\partial j_r}{\partial z} + \hat{\boldsymbol{\phi}} \frac{\partial j_\phi}{\partial z} + \hat{\boldsymbol{z}} \frac{\partial j_z}{\partial z} \right) \\ = \quad & -ik (\boldsymbol{\nabla} \times \boldsymbol{B}), \end{aligned} \tag{A12}$$

where we have exploited that $\boldsymbol{\nabla} \times \boldsymbol{B} = \mu_0 \boldsymbol{j}$ is of the form in Eq. A1 such that Eq. A3 applies. Applying triple product expansion to the third term in Eq. A10 yields

$$\begin{aligned} \boldsymbol{\nabla} n \times [\hat{\boldsymbol{z}} \times (\boldsymbol{\nabla} \times \boldsymbol{B})] = \quad & \hat{\boldsymbol{z}} [\boldsymbol{\nabla} n \cdot (\boldsymbol{\nabla} \times \boldsymbol{B})] \\ & - (\boldsymbol{\nabla} \times \boldsymbol{B}) (\boldsymbol{\nabla} n \cdot \hat{\boldsymbol{z}}), \end{aligned} \tag{A13}$$

where the second term vanishes since $\boldsymbol{\nabla} n \perp \hat{\boldsymbol{z}}$. Eq. A10 then becomes

$$ik_w^2 \boldsymbol{B} = \quad iks(\boldsymbol{\nabla}\times\boldsymbol{B}) - i\delta\boldsymbol{\nabla}\times(\boldsymbol{\nabla}\times\boldsymbol{B}) + \frac{s}{n}\left[\boldsymbol{\nabla} n\cdot(\boldsymbol{\nabla}\times\boldsymbol{B})\right]\hat{\boldsymbol{z}} + \frac{i\delta}{n}\boldsymbol{\nabla} n\times(\boldsymbol{\nabla}\times\boldsymbol{B}), \tag{A14}$$

where we have used the definition $k_w^2 = \mu_0 en\omega/B_0$. Lastly Eq. A14 can be recast into

$$\delta\boldsymbol{\nabla}\times(\boldsymbol{\nabla}\times\boldsymbol{B}) - ks(\boldsymbol{\nabla}\times\boldsymbol{B}) + k_w^2\boldsymbol{B} = -is\hat{\boldsymbol{z}}\left[\frac{\boldsymbol{\nabla} n}{n}\cdot(\boldsymbol{\nabla}\times\boldsymbol{B})\right] + \delta\frac{\boldsymbol{\nabla} n}{n}\times(\boldsymbol{\nabla}\times\boldsymbol{B}), \tag{A15}$$

which after back-substituting $s = \pm$ is the sought after wave equation shown in Eq. 5. Since δ is of order 10^{-2} or smaller - e.g. $9.7\cdot10^{-3}$ at 13.56 MHz and 50 mT - the second source term is negligible. Further, since $\boldsymbol{\nabla} n \| \hat{\boldsymbol{r}}$, by means of Eq. A2 and A3 the source simplifies into the alternate form

$$\mp i\left[\frac{\boldsymbol{\nabla} n}{n}\cdot(\boldsymbol{\nabla}\times\boldsymbol{B})\right]\hat{\boldsymbol{z}} = \pm\frac{1}{n}\frac{\partial n}{\partial r}\left(\frac{mB_z}{r} - kB_\phi\right)\hat{\boldsymbol{z}}, \tag{A16}$$

which for comparable strength of B_z and B_ϕ and $r^{-1} \gg k$ becomes the expression shown in Eq. 7. Alternatively, since $\boldsymbol{\nabla}\times\boldsymbol{B} = \mu_0\boldsymbol{j}$, the source for a purely radial density gradient becomes

$$\mp i\left[\frac{\boldsymbol{\nabla} n}{n}\cdot(\boldsymbol{\nabla}\times\boldsymbol{B})\right]\hat{\boldsymbol{z}} = \mp\frac{i\mu_0}{n}\frac{\partial n}{\partial r}j_r\hat{\boldsymbol{z}}, \tag{A17}$$

as shown previously in Eq. 8.

Appendix B: Symbols used in this Work

Symbol	Description
m	azimuthal mode/wave number
k	axial wave number
ω	whistler/helicon wave frequency [rad/s]
$\boldsymbol{E}$	electric wavefield components
$\boldsymbol{B}$	magnetic wavefield components
$\boldsymbol{j}$	wavefield currents
B_0	background magnetic field magnitude
s	direction of magnetic background field (Eq. A4)
n	electron density
$\boldsymbol{v}$	electron velocity
T_e	electron temperature
ν	effective combined electron-ion and electron-neutral collision frequency
δ	ratio of whistler to electron-cyclotron frequency (Eq. 6)
k_w	$\sqrt{\mu_0 en\omega/B_0}$ (Eq. 6)

REFERENCES

[1] R. W. Boswell, "Very efficient plasma generation by whistler waves near the lower hybrid frequency," Plasma Physics and Controlled Fusion **26**, 1147–1162 (1984).

[2] F. F. Chen, "Plasma ionization by helicon waves," Plasma Physics and Controlled Fusion **33**, 339–364 (1991).

[3] P. Aigrain, "Les 'helicons' dans les semiconducteurs," in *Intl. Conf. on Semiconductor Physics* (1960) p. 224.

[4] B. Maxfield, "Helicon waves in solids," American Journal of Physics **37**, 241–269 (1969).

[5] J. A. Lehane and P. C. Thonemann, "An experimental study of helicon wave propagation in a gaseous plasma," Proceedings of the Physical Society **85**, 301–316 (1965).

[6] L. C. Woods, "Hydromagnetic waves in a cylindrical plasma," Journal of Fluid Mechanics **13**, 570–586 (1962).

[7] J. P. Klozenberg, B. Mcnamara, and P. C. Thonemann, "The dispersion and attenuation of helicon waves in a uniform cylindrical plasma," Journal of Fluid Mechanics **21**, 545–563 (1965).

[8] R. Stenzel, "Whistler waves in space and laboratory plasmas," Journal of Geophysical Research: Space Physics **104**, 14379–14395 (1999).

[9] P. Zarka, "Radio and plasma waves at the outer planets," Advances in Space Research **33**, 2045–2060 (2004).

[10] R. Strangeway, "Plasma waves at venus," Space science reviews **55**, 275–316 (1991).

[11] B. Buttenschön, N. Fahrenkamp, and O. Grulke, "A high power, high density helicon discharge for the plasma wakefield accelerator experiment AWAKE," Plasma Physics and Controlled Fusion **60** (2018), 10.1088/1361-6587/aac13a.

[12] G. R. Tynan, A. D. Bailey, G. A. Campbell, R. Charatan, A. de Chambrier, G. Gibson, D. J. Hemker, K. Jones, A. Kuthi, C. Lee, T. Shoji, and M. Wilcoxson, "Characterization of an azimuthally symmetric helicon wave high density plasma source," Journal of Vacuum Science & Technology A: Vacuum, Surfaces, and Films **15**, 2885–2892 (1997).

[13] J. P. Squire, F. R. Chang-Díaz, T. W. Glover, V. T. Jacobson, G. E. McCaskill, D. S. Winter, F. W. Baity, M. D. Carter, and R. H. Goulding, "High power light gas helicon plasma source for VASIMR," Thin Solid Films **506-507**, 579–582 (2006).

[14] J. Rapp, T. M. Biewer, T. S. Bigelow, J. B. Caughman, R. C. Duckworth, R. J. Ellis, D. R. Giuliano, R. H. Goulding, D. L. Hillis, R. H. Howard, T. L. Lessard, J. D. Lore, A. Lumsdaine, E. J. Martin, W. D. McGinnis, S. J. Meitner, L. W. Owen, H. B. Ray, G. C. Shaw, and V. K. Varma, "The Development of the Material Plasma Exposure Experiment," IEEE Transactions on Plasma Science **44**, 3456–3464 (2016).

[15] J. Rapp, T. M. Biewer, T. S. Bigelow, J. F. Caneses, J. B. Caughman, S. J. Diem, R. H. Goulding, R. C. Isler, A. Lumsdaine, C. J. Beers, T. Bjorholm, C. Bradley, J. M. Canik, D. Donovan, R. C. Duckworth, R. J. Ellis, V. Graves, D. Giuliano, D. L. Green, D. L. Hillis, R. H. Howard, N. Kafle, Y. Katoh, A. Lasa, T. Lessard, E. H. Martin, S. J. Meitner, G. N. Luo, W. D. McGinnis, L. W. Owen, H. B. Ray, G. C. Shaw, M. Showers, and V. Varma, "Developing the science and technology for the Material Plasma Exposure eXperiment," Nuclear Fusion **57** (2017), 10.1088/1741-4326/aa7b1c.

[16] E. Gschwendtner, E. Adli, L. Amorim, R. Apsimon, R. Assmann, A.-M. Bachmann, F. Batsch, J. Bauche, V. B. Olsen, M. Bernardini, *et al.*, "Awake, the advanced proton driven plasma wakefield acceleration experiment at cern," Nuclear Instruments and Methods in Physics Research Section A: Accelerators, Spectrometers, Detectors and Associated Equipment **829**, 76–82 (2016).

[17] I. Adamovich, S. Agarwal, E. Ahedo, L. L. Alves, S. Baalrud, N. Babaeva, A. Bogaerts, A. Bourdon, P. Bruggeman, C. Canal, *et al.*, "The 2022 plasma roadmap: low temperature plasma science and technology," Journal of Physics D: Applied Physics **55**, 373001 (2022).

[18] T. V. Tsankov, P. Chabert, and U. Czarnetzki, "Foundations of magnetized radio-frequency discharges," Plasma Sources Science and Technology **31**, 084007 (2022).

[19] T. H. Stix, *Waves in plasmas* (Springer Science & Business Media, 1992).

[20] V. Karpman and R. Kaufman, "Whistler wave propagation in density ducts,"

Journal of Plasma Physics **27**, 225–238 (1982).
[21] R. Chen, X. Gao, Q. Lu, L. Chen, B. T. Tsurutani, W. Li, B. Ni, and S. Wang, "In situ observations of whistler-mode chorus waves guided by density ducts," Journal of Geophysical Research: Space Physics **126**, e2020JA028814 (2021).
[22] F. F. Chen, "Helicon discharges and sources: A review," Plasma Sources Science and Technology **24** (2015), 10.1088/0963-0252/24/1/014001.
[23] M. Light and F. F. Chen, "Helicon wave excitation with helical antennas," Physics of Plasmas **2**, 1084–1093 (1995).
[24] D. G. Miljak and F. F. Chen, "Helicon wave excitation with rotating antenna fields," Plasma Sources Science and Technology **7**, 61–74 (1998).
[25] I. D. Sudit and F. F. Chen, "Discharge equilibrium of a helicon plasma," Plasma Sources Science and Technology **5**, 43–53 (1996).
[26] S. Shinohara and T. Tanikawa, "Development of very large helicon plasma source," Review of Scientific Instruments **75**, 1941–1946 (2004).
[27] J. Green and O. Schmitz, "Construction of a linear plasma device for studying helicon plasmas relevant to plasma-wakefield accelerators," Plasma Sources Science and Technology **29** (2020), 10.1088/1361-6595/ab7852.
[28] S. C. Thakur, C. Brandt, L. Cui, J. J. Gosselin, and G. R. Tynan, "Formation of the Blue Core in Argon Helicon Plasma," IEEE Transactions on Plasma Science **43**, 2754–2759 (2015).
[29] R. F. Boivin, J. L. Kline, and E. E. Scime, "Electron temperature measurement by a helium line intensity ratio method in helicon plasmas," Physics of Plasmas **8**, 5303–5314 (2001).
[30] D. D. Blackwell and F. F. Chen, "Two-dimensional imaging of a helicon discharge," Plasma Sources Science and Technology **6**, 569–576 (1997).
[31] A. W. Degeling, C. O. Jung, R. W. Boswell, and A. R. Ellingboe, "Plasma production from helicon waves," Physics of Plasmas **3**, 2788–2796 (1996).
[32] Y. T. Sung, Y. Li, and J. E. Scharer, "Fast, hot electron production and ion acceleration in a helicon inductive plasma," Physics of Plasmas **23**, 1–9 (2016).
[33] R. M. Magee, M. E. Galante, J. Carr, G. Lusk, D. W. McCarren, and E. E. Scime, "Neutral depletion and the helicon density limit," Physics of Plasmas **20**, 1–6 (2013).
[34] K. K. Chi, T. E. Sheridan, and R. W. Boswell, "Resonant cavity modes of a bounded helicon discharge," Plasma Sources Science and Technology **8**, 421–431 (1999).
[35] M. M. Balkey, R. Boivin, J. L. Kline, and E. E. Scime, "Ion heating and density production in helicon sources near the lower hybrid frequency," Plasma Sources Science and Technology **10**, 284–294 (2001).
[36] M. Afsharmanesh and M. Habibi, "Development of a helicon ion source: Simulations and preliminary experiments," Review of Scientific Instruments **89** (2018), 10.1063/1.5010010.
[37] P. A. Piotrowicz, J. F. Caneses, D. L. Green, R. H. Goulding, C. Lau, J. B. Caughman, J. Rapp, and D. N. Ruzic, "Helicon normal modes in Proto-MPEX," Plasma Sources Science and Technology **27** (2018), 10.1088/1361-6595/aabd62.
[38] P. Guittienne, E. Chevalier, and C. Hollenstein, "Towards an optimal antenna for helicon waves excitation," Journal of Applied Physics **98** (2005), 10.1063/1.2081107.
[39] S. Dujko, D. Bošnjaković, R. White, and Z. L. Petrović, "Heating mechanisms for electron swarms in radio-frequency electric and magnetic fields," Plasma Sources Science and Technology **24**, 054006 (2015).
[40] J. Green, O. Schmitz, and M. Zepp, "Direct measurement of the ionization source rate and closure of the particle balance in a helicon plasma using laser induced fluorescence," Physics of Plasmas **27**, 043511 (2020).
[41] F. F. Chen and D. Arnush, "Generalized theory of helicon waves. I. Normal modes," Physics of Plasmas **4**, 3411–3421 (1997).
[42] D. Arnush, "The role of trivelpiece-gould waves in antenna coupling to helicon waves," Physics of Plasmas **7**, 3042–3050 (2000).
[43] F. F. Chen and D. D. Blackwell, "Upper limit to landau damping in helicon discharges," Phys. Rev. Lett. **82**, 2677–2680 (1999).
[44] D. Arnush and F. F. Chen, "Generalized theory of helicon waves. II. Excitation and absorption," Physics of Plasmas **5**, 1239–1254 (1998).
[45] F. F. Chen, "Physics of helicon discharges," Physics of Plasmas **3**, 1783–1793 (1996).
[46] T. Watari, T. Hatori, R. Kumazawa, S. Hidekuma, T. Aoki, T. Kawamoto, M. Inutake, S. Hiroe, A. Nishizawa, K. Adati, T. Sato, T. Watanabe, H. Obayashi, and K. Takayama, "Radio-frequency plugging of a high density plasma," Physics of Fluids **21**, 2076–2081 (1978).